Quantitative Characterization and Mechanism of Formation of Multilength-scale Bulk Heterojunction Structures in Highly Efficient Solution-Processed Small-Molecule Organic Solar Cel...

10 AUTHORS, INCLUDING:

Yu-Ching Huang
Institute of Nuclear Energy Research
34 PUBLICATIONS   438 CITATIONS

SEE PROFILE

Cheng-Si Tsao
Institute of Nuclear Energy Research
40 PUBLICATIONS   702 CITATIONS

SEE PROFILE

Hou-Chin Cha
Institute of Nuclear Energy Research
24 PUBLICATIONS   253 CITATIONS

SEE PROFILE

Chih Wei Chu
Academia Sinica
169 PUBLICATIONS   4,487 CITATIONS

SEE PROFILE

Quantitative Characterization and Mechanism of Formation of Multilength-scale Bulk Heterojunction Structures in Highly Efficient Solution-Processed Small-Molecule Organic Solar Cells

Yu-Ching Huang,[†] Cheng-Si Tsao,*,[†] Tzu-Yen Huang,[‡,§] Hou-Chin Cha,[†] Dhananjaya Patra,[‡] Chun-Jen Su,[⊥] U-Ser Jeng,[⊥] Kuo-Chuan Ho,[§] Kung-Hwa Wei,[∥] and Chih-Wei Chu*,[‡]

[†]Institute of Nuclear Energy Research, Longtan, Taoyuan 32546, Taiwan
[‡]Research Center for Applied Sciences, Academia Sinica, Taipei, Taiwan
[§]Department of Chemical Engineering, National Taiwan University, Taipei, Taiwan
[⊥]National Synchrotron Radiation Research Center, Hsinchu 30077, Taiwan
[∥]Department of Materials Science and Engineering, National Chiao-Tung University, Hsinchu, Taiwan

S *Supporting Information*

ABSTRACT: In this study we used simultaneous grazing-incidence small- and wide-angle X-ray scattering (GISAXS and GIWAXS, respectively) to probe the multilength-scale structures of thin active layers comprising the linear A−D−A-type π-conjugated donor molecule TBDTCNR and the fullerene acceptor molecule $PC_{61}BM$ for use in solution-processed small-molecule-based organic solar cells (SMOSCs). We found that the pseudo-two-dimensional fractal-like networks in the bulk heterojunction (BHJ) structure were determined by mutual interactions between the small-molecule (SM) crystallites and the nanoscale $PC_{61}BM$ clusters during their formation and phase separation, and deduced quantitatively, at multiple length scales, the BHJ structures comprising these SM crystallites and $PC_{61}BM$ clusters. We also conducted in situ GIWAXS measurements to study the temporal behavior and kinetics of SM crystallization from solution to the solid film state. Our GISAXS/GIWAXS study revealed that the multilength-scale BHJ structures in the thin films could be tuned effectively by varying the amount of incorporated $PC_{61}BM$ and the annealing temperature. This study provides fundamental information relating to the mechanism of formation of hierarchical BHJ structures through relatively rapid crystallization of a highly crystalline SM, as well as the relationships among the hierarchical structure, the photovoltaic performance, and the mechanism of formation, thereby allowing greater control over BHJ structures in SMOSCs with optimized fabrication and performance.
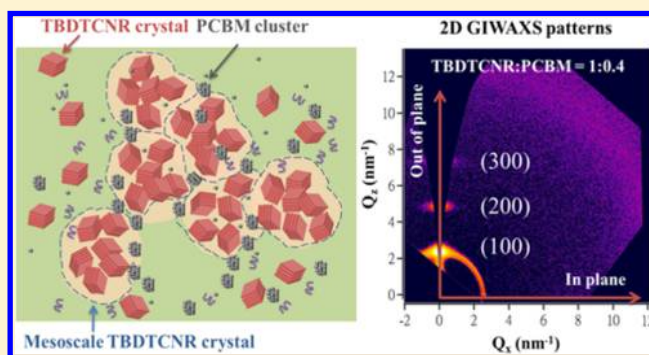
1. INTRODUCTION

Solution-processed organic solar cells (OSCs) have become a promising next-generation photovoltaic technology because of their low cost, simple fabrication, high-throughput, relatively short energy payback time,[1] large-area production through roll-to-roll processing, and mechanical flexibility.[2−4] Recently, the development of solution-processed small-molecule−based organic solar cells (SMOSCs) has progressed to such an extent that their power conversion efficiencies (PCEs) have reached 8%,[5−7] comparable with those (>9%) of polymer-based solar cells (PSCs).[8] Moreover, SMOSCs have several advantages over PSCs, including well-defined molecular structures, higher purity,[9] higher crystallinity in the active layer, higher open-circuit voltages for devices, and lower batch-to-batch variation,[10,11] resulting in their becoming competitive with PSCs.

One of the most critical factors affecting the photovoltaic performance of all-solution-processed OSCs is the bulk heterojunction (BHJ) structure (i.e., the nanometer-scale morphology of the active layer).[12−28] On the basis of previous reports,[6,29,30] it appears that the short-circuit current, which depends on the rational BHJ design, is the critical photovoltaic property of SMOSCs. Research into the fundamental effects of the BHJ structures of SMOSCs is, however, limited, and remains lagging behind that of PSCs.

The three-dimensional (3D) self-organized BHJ nanostructures that form through phase separation of blends of organic molecules and fullerenes are complicated multilength-scale structures. The self-organization of a polymer or small organic

molecule (as donor) into crystallites governs exciton generation and subsequent charge separation at the interface and also serves as the pathway for the transport of the holes, substantially affecting the PCEs of corresponding devices. On the other hand, the aggregation of [6,6]-phenyl-C_{61}-butyric acid methyl ester ($PC_{61}BM$; as acceptor) into clusters provides the path for electron transport. The spatial locations of nanoscale phase-separated donor crystal and acceptor cluster domains in a BHJ thin film can constitute an interpenetrating (or bicontinuous) network for effective separation and subsequent transport of charge carriers toward their respective electrodes; thus, miscibility between the acceptor and donor molecules plays an important role in the determination of the extent of separation and, therefore, affects the transport of charge carriers.[6,29−33] In the past few years, simultaneous grazing-incidence small-angle and wide-angle X-ray scattering (GI-SAXS/GIWAXS) has been used as a powerful tool for quantitatively elucidating multilength-scale structures in polymer/fullerene thin films of BHJ solar cells, in conjunction with conventional microscopic and simple X-ray diffraction (XRD) techniques.[15−21] GISAXS and GIWAXS provide complementary microscopic insight into complex hierarchical structures, as reported in several recent reviews.[34−37] To date, studies of the BHJ structures of solution-processed SMOSCs have focused mainly on real-space observations using atomic force microscopy (AFM), transmission electron microscopy (TEM), and XRD techniques, which have the limitations of allowing qualitative analyses on only the nano- and mesoscales. In addition, there have been very few studies using GIWAXS or GISAXS to determine the phase-separated structures of SMOSCs with the $PC_{71}BM$ acceptor.[38,39] In the recent literatures, the charge transfer process in the BHJ structure of SMOSCs was investigated by the theoretical calculation[40,41] and analyzed by the general approaches, like impedance spectra and photoluminescence spectra etc.[42−46] However, the directly experimental data between charge transfer and BHJ structure was still lack because of the difficult of structural characterization. The study of multilength-scale BHJ structure of SMOSCs can provide the critical information.

When forming BHJ structures, the modes of molecular packing of the small molecules (SMs) to form localized high-crystallinity structures as well as the aggregation of the fullerene can lead to interpenetration networks of the acceptor/donor components and phase separation mechanisms that differ substantially from those of BHJ PSCs (discussed below). Quantitative analyses of multilength-scale BHJ structures in thin films and a mechanistic understanding of the factors controlling the nanoscale phase separation not only are of high academic interest but are also critical to the design and fabrication of highly efficient solution-processed SMOSCs. To the best of our knowledge, this paper describes the first use of simultaneous GISAXS and GIWAXS for quantitative characterization of the multilength-scale structures and spatial distributions of nanophase-separated donor and acceptor ($PC_{61}BM$-based) units in the 3D structures of solution-processed SMOSCs. We also establish herein a SAXS analysis model for successfully resolving the multilength-scale structures of the donor and acceptor phases in solution-processed SMOSCs at different scale levels. $PC_{61}BM$ and $PC_{71}BM$ have different miscibilities with the donor material in the blend film, leading to different degrees of SM crystallization and different BHJ structures. The general literature[47] reports that the additive in the SM:$PC_{71}BM$ films can increase the content of

high degree of crystallization SM crystallites and enhance the BHJ structure. The blend films of $PC_{71}BM$ and the SM synthesized in this present study also displayed a similar trend in performance (Supporting Information). The structural changes and characteristic behavior of SM:$PC_{61}BM$ SCs are, however, different from those of SM:$PC_{71}BM$ SCs. The additive and the thermal treatment performed in this present study destroyed the SM's crystallinity and produced an unfavorable BHJ structure. We studied the SM:$PC_{61}BM$ SCs to obtain a comprehensive understanding of the structural control and process design of such SM:fullerene derivative systems.

We used TBDTCNR, a linear A−D−A-type π-conjugated donor molecule comprising a planar electron-rich 2-octylthiene-5-yl−substituted benzodithiophene (TBDT) core unit, flanked by octylthiophene units, and end-capped with an electron-deficient cyanoacetate (CNR) unit, as our donor material. The TBDT core has a sulfur-rich, electron-donating coplanar structure; therefore, is can undergo π-stacking interactions, resulting in high mobility and excellent SMOSC performance relative to that of PSCs.[48] An OSC device incorporating a TBDTCNR:$PC_{61}BM$ blend as an active layer has been reported previously to exhibit a high PCE.[32] In this study we structurally characterized TBDTCNR:$PC_{61}BM$ blend films in terms of their (i) orientational distribution, relative crystallinity, and ordered structures of nanoscale edge-on and face-on molecular crystallites; (ii) size and spatial distributions of nanoscale $PC_{61}BM$ clusters; (iii) mesoscale structures formed from aggregated molecular crystallites; and (iv) TBDTCNR/$PC_{61}BM$ miscible domains or matrix.[6,31,49] On the basis of these characteristics, we could propose the spatial distributions or frameworks of the interpenetrating TBDTCNR/$PC_{61}BM$ networks. To investigate how the $PC_{61}BM$ clusters mutually interacted with and/or were confined (or governed) by the molecular domains, we analyzed the evolution of phase-separated multilength-scale structures in the blend films as functions of the donor/acceptor ratio and the annealing temperature, respectively, to provide a framework for determining the mechanism of formation. We did not observe the additive effect on the TBDTCNR/$PC_{61}BM$ SMOSC because of low degree of SM crystallization. We also observed the formed films in real space using TEM and AFM, which provided complementary information on different scales. Finally, we correlated the optimal BHJ structures with the performance and mobility of the SMOSC-based devices by determining the relationships among the structure, properties, and processing conditions. Accordingly, we obtained a detailed mechanistic understanding of phase separation on different length scales; this fundamental information could be used to tailor the structures of high-performance SMOSCs.

2. EXPERIMENTAL SECTION

2.1. Preparation and Characterization of TBDTCNR:$PC_{61}BM$ Blend Films. The synthesis of TBDTCNR as the donor has been described in detail previously.[32] Similar to the conditions for preparing the active layers of the solution-processed SM BHJ blend films, the samples for synchrotron scattering experiments were prepared through spin-casting of blend solutions of TBDTCNR and $PC_{61}BM$ (as the acceptor) on Si substrates (2 cm ×1 cm). The active layer solution comprised TBDTCNR and $PC_{61}BM$ in $CHCl_3$ (concentration of donor materials: 8 mg mL^{-1}); details of the preparation procedure have been reported elsewhere.[32]

The active layers, prepared at TBDTCNR:PC$_{61}$BM weight ratios of 1:0.4, 1:0.75, and 1:0.9, were annealed at room temperature for 30 min under a nitrogen environment in the glovebox. For the film prepared at a 1:0.4 weight blend ratio, thermal annealing was performed at 75, 100, or 125 °C for 30 min to preanneal the active layer. A pristine TBDTCNR thin film was also prepared at room temperature as a reference. The thickness of each active layer was measured using an Alpha Step profilometer (Veeco, Dektak 150).

Corresponding SMOSC devices based on these films were fabricated with the structure indium tin oxide (ITO) glass/poly(3,4-ethylenedioxythiophene):polystyrenesulfonate (PEDOT:PSS)/TBDTCNR:PC$_{61}$BM BHJ active layer/Ca/Al. Preannealing was performed prior to thermal deposition of the metal cathode. Voltage−photocurrent curves of these solar cells were measured under A.M. 1.5 illumination (100 mW cm^{-2}) using a solar simulator (Thermal Oriel 1000W). The device area, defined by the area of the Ca/Al electrode, was 0.1 cm^2. The configurations of the hole- and electron-only devices were ITO glass/PEDOT:PSS/TBDTCNR:PC$_{61}$BM/V$_2$O$_5$/Al and ITO glass/Cs$_2$CO$_3$/TBDTCNR:PC$_{61}$BM/Ca/Al, respectively. The electron and hole motilities were determined by fitting the plots of the dark J−V curves for single-carrier devices to the space-charge-limited current (SCLC) model. AFM and TEM were employed to study the BHJ morphologies of the active layers. The devices and blend films annealed at room temperature retained their stable performance and structures when maintained at room temperature for long periods of time.

2.2. Simultaneous GISAXS/GIWAXS Experiments for TBDTCNR:PC$_{61}$BM Blend Films. Simultaneous GISAXS and GIWAXS measurements for all polymer/fullerene blend films, prepared at various blend ratios and annealing temperatures, were performed at beamline 23A of the National Synchrotron Radiation Research Center (NSRRC), Taiwan. Previous studies have revealed that the morphologies and GISAXS/GIWAXS intensities produced by active layers are unaffected by the presence of silicon and ITO/PEDOT:PSS substrates.[17,33] The scattering intensities of the TBDTCNR/PC$_{61}$BM blend film cast on the Si/PEDOT:PSS substrate were almost identical to those of the blend film cast on a Si substrate. The PEDOT:PSS substrate effect can be considered as minor effect and was not reflected by the scattering data (Supporting Information). In the GISAXS/GIWAXS measurements, the incident angle to each thin film was aligned precisely to 0.2 ± 0.002°. The incident angle is well above all critical angles of the involved materials and slightly less than the critical angle of Si substrate, allowing penetration through the whole active layer. Two-dimensional (2D) GISAXS or GIWAXS patterns were collected simultaneously from two 2D detectors located at different positions. The instrument configuration and experimental procedure have been described previously.[20] One-dimensional (1D) GISAXS profiles as a function of the scattering vector Q_x were reduced along the in-plane direction of the 2D GISAXS patterns (parallel to the substrate or film surface; defined as the X direction). The measured 1D GISAXS data covered the region of the Yoneda peak. The conventional SAXS model is still available to analyze the Yoneda peak reduced from 2D GISAXS pattern without considering the distorted wave Born approximation.[37,50] The measured 2D GIWAXS patterns were corrected with consideration of the geometric effect.[36,51] The GIWAXS data were corrected for background. The 1D out-of-plane GIWAXS profiles were reduced along the out-of-plane direction of the 2D GIWAXS patterns (perpendicular to the substrate or film surface; defined as the Z direction) and are expressed as a function of scattering vector Q_z. A cake slice was taken [polar angle (χ): 0−20°] for analysis of the full out-of-plane (100) diffraction spot and the other spots. The 1D in-plane GISAXS profiles as a function of Q_x were reduced along the in-plane direction of the 2D GIWAXS pattern. A cake slice was taken (χ: 75−90°) for the analysis of the in-plane (100) diffraction spot.

3. RESULTS AND DISCUSSION

### 3.1. Nanoscale BHJ Structure of TBDTCNR/PC$_{61}$BM Blend Films: GISAXS Analysis. Figure 1a presents in-plane
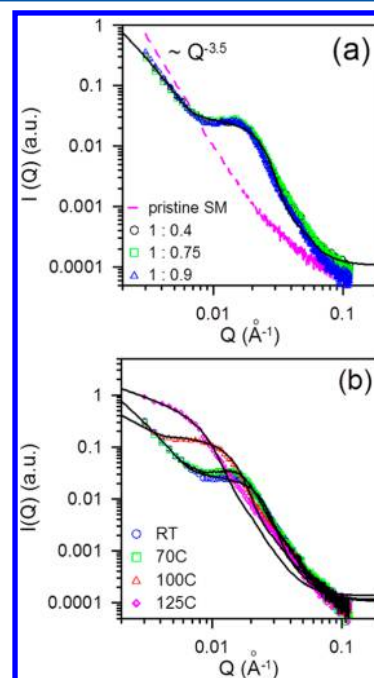
Figure 1. GISAXS profiles of (a) room-temperature-annealed TBDTCNR:PC61BM blend films prepared at weight ratios of 1:0 (pristine), 1:0.4, 1:0.75, and 1:0.9 and (b) TBDTCNR:PC61BM (1:0.4) blend films annealed at room temperature and 75, 100, and 125 °C. All of the profiles were fitted well with calculated modeled intensities (solid lines).

GISAXS profiles for the room-temperature-annealed BHJ films prepared at TBDTCNR:PC$_{61}$BM weight blend ratios of 1:0.4, 1:0.75, and 1:0.9. Although the shapes of the GISAXS profiles were somewhat similar to those of solution-processed BHJ PSCs reported previously,[16,19,20,33−35,37] the structures and mechanisms of formation of the active layers in the SMOSCs behind these GISAXS profiles were completely different from those of conventional PSCs. First, the GISAXS profile of the pristine TBDTCNR film (Figure 1) exhibited high intensity with power-law scattering $[I(Q) \sim Q^{-n}]$ behavior with a value of n of 3.5, suggesting a fractal surface ($3 < n < 4$) of large molecular crystallites on the micrometer scale.[52−55] Compared with the very weak and negligible intensities in the GISAXS profiles of well-known P3HT polymer crystallites in PSCs, this GISAXS profile provides direct evidence for a high degree of crystallization arising from the nature of the SM, consistent with the data we obtained through GIWAXS (Figure 2). Our GISAXS/GIWAXS results confirmed that the crystallization behavior of TBDTCNR is different from that reported previously from thermal-annealing-enhanced SM crystallization
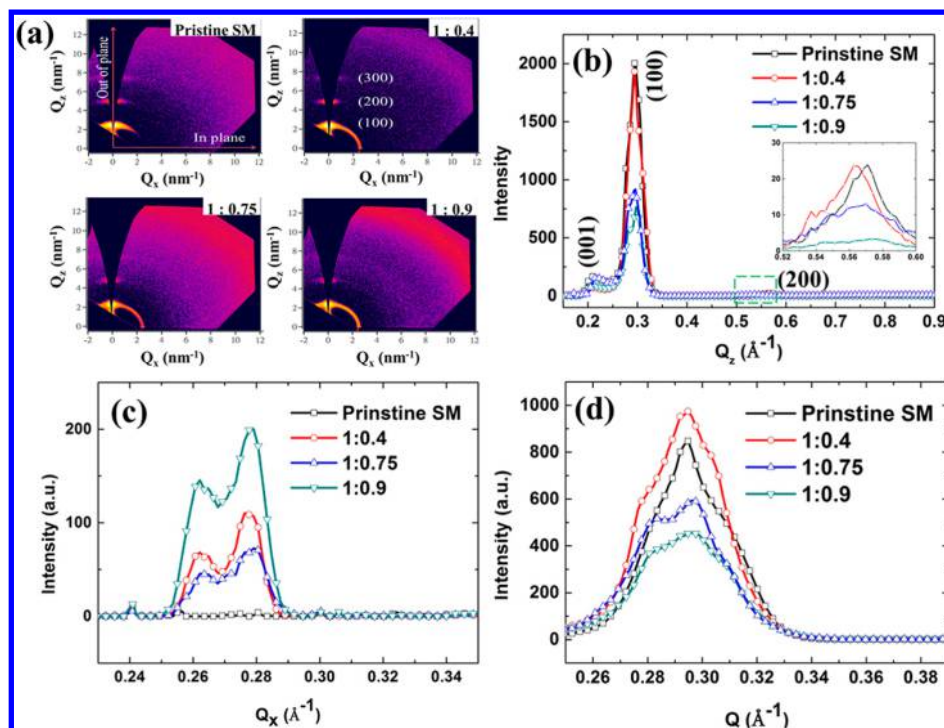
Figure 2. (a) 2D GIWAXS patterns, (b) out-of-plane GIWAXS profiles, (c) in-plane GIWAXS profiles, and (d) ring-averaged GIWAXS profiles for TBDTCNR:$PC_{61}BM$ blend films prepared at weight ratios of 1:0 (pristine), 1:0.4, 1:0.75, and 1:0.9.

in another GIWAXS study.[39] The literature[39] reports that SM crystallization in the pristine film and the blend film with $PC_{71}BM$ began at temperatures above 50 °C (i.e., cold crystallization temperatures). The crystallization of the SM prepared in this present study began at room temperature.

After $PC_{61}BM$ molecules had been incorporated into the film, a broad peak or shoulder (at 0.008−0.03 Å^{-1}) appeared in the medium-Q region of the GISAXS profiles [Figure 1 (a)], in addition to the scattering shape arising from the original crystallization. We attribute this signal to the aggregation of $PC_{61}BM$ molecules into nanoscale clusters. As reported previously,[16,19,20,33] the GISAXS intensity corresponding to this $I(Q)_{PCBM}$ peak can be modeled using a polydisperse sphere model having Schulz size distribution, with hard-sphere interactions between $PC_{61}BM$ clusters:

$$I_{PCBM}(Q) = \eta V(\Delta \rho)^2 \Big[\int_0^\infty F_i(Q, \sigma_i)^2 f(\sigma_i) \, d\sigma_i$$
$$+ \int_0^\infty \int_0^\infty F_i(Q, \sigma_i) F_j(Q, \sigma_j) H_{ij}(Q, \sigma_i, \sigma_j)$$
$$f_i(\sigma_i) f_j(\sigma_j) \, d\sigma_i \, d\sigma_j \Big] \qquad (1)$$

where $F(Q, \sigma_I)^2$ is the form factor of a spherical $PC_{61}BM$ cluster having a diameter σ_i; $H(Q, \sigma_i, \sigma_j)$ is the pair structure function describing the interaction between clusters with a Percus−Yevick approximation for hard-sphere interactions; V is the average cluster volume; and $\Delta \rho$ is the scattering length density contrast between the $PC_{61}BM$ cluster and the matrix. The fitting parameters η, R, and p are the volume fraction, mean radius, and polydispersity of the size distribution of the $PC_{61}BM$ clusters, respectively; the polydispersity, p, is defined as a/R, where a^2 is the variance of the Schulz size distribution $f(\sigma)$. The volume fraction η, a nonlinear parameter in the pair structure function, can be obtained by model-fitting of the peak shape and peak position located at the mid-Q region (not only

a constant as prefactor). The extracted value of η can serve as a roughly relative reference. Accurate determination of the volume fraction was very difficult in this study because of several uncertainties (e.g., uncertainty in the probed volume).

3.2. Mesoscale BHJ Structure of Blend Films: A Combination of GISAXS and GIWAXS Analysis. Moreover, the intensity upturn in the low-Q region (0.003−0.008 Å^{-1}) for the TBDTCNR:$PC_{61}BM$ blend films also exhibited a power-law scattering with a value of n of 2.5. Notably, the exponent of power-law scattering changed from a surface fractal regime for the pristine TBDTCNR film to a mass fractal regime ($1 < n < 3$) for the blend films,[52−54] suggesting the formation of a fractal network of SM crystallites comprising aggregates of several mesoscale crystallites as primary particles (confirmed through subsequent quantitative analysis; see below). We speculated that the micrometer-scale SM crystallites (originally existing in the pristine SM film) were disrupted to form a fractal-like network (in some scales) as a result of the incorporation of $PC_{61}BM$ molecules or the dispersion of $PC_{61}BM$ clusters. In addition, the corresponding GIWAXS profiles featured the (100) diffraction peak arising from the lamellar structure of single TBDTCNR crystals (Figure 2). From the peak width and the Scherrer equation, we estimated the size of the single SM crystals to be approximately 18 nm. On the basis of the GIWAXS data, we further deduced that the mesoscale primary SM crystallites formed through closely packed aggregation of nanoscale single SM crystals (ca. 18 nm). If the aggregated single SM crystals were not closely packed, the GISAXS spectra should have revealed the existence of nanoscale single SM crystals. Notably, the fractal-like network formed through the crystallization of the SMs investigated herein was distinctively different from the structure of crystallized P3HT; nanoscale single P3HT crystals usually aggregate into fibril- or nodule-like P3HT crystals with macroscale or mesoscale lengths (they can

be regarded as loose aggregates of nanoscale P3HT crystals with noncontact form).[37]

According to the literature,[36] the relative degree of crystallinity (r_{DOC}) of the SMs in the film can be roughly estimated from the azimuthally integrated intensity of the (100) diffraction peak (ring) over polar angles ranging from 0 to 90°. The r_{DOC} of the SMs in the blend films decreased gradually upon increasing the weight ratio of $PC_{61}BM$ in the blend from 0.4 to 0.75 or 0.9 (as revealed by the peak area or intensity height of the (100) diffraction peak in the GIWAXS profile; see Figure 2d). This behavior implies, once again, that a greater number of $PC_{61}BM$ molecules dispersed in the matrix results in a lower degree of SM crystallization (i.e., the presence of $PC_{61}BM$ interfered with the nucleation sites of the SM crystallites). Because the fractal network of SM crystallites formed through aggregation of mesoscale primary SM crystallites was independent of the content of incorporated $PC_{61}BM$ molecules (as evidenced by the low-Q GISAXS intensity in Figure 1), we speculate that the decrease in the degree of crystallization was caused by the decrease in the content of nanoscale single SM crystals dispersed in the matrix domain, implying that the amorphous matrix (i.e., a miscible domain) comprised individually dispersed $PC_{61}BM$ molecules and SM molecules intermixed with some nanoscale SM crystallites. Thus, a fraction of the single SM crystallites existed in the amorphous matrix, rather than aggregated into a network. Figure 3 provides a schematic representation of the multilength-scale structure of the acceptor and donor phases that is consistent with the results of our simultaneous GISAXS/GIWAXS analyses.
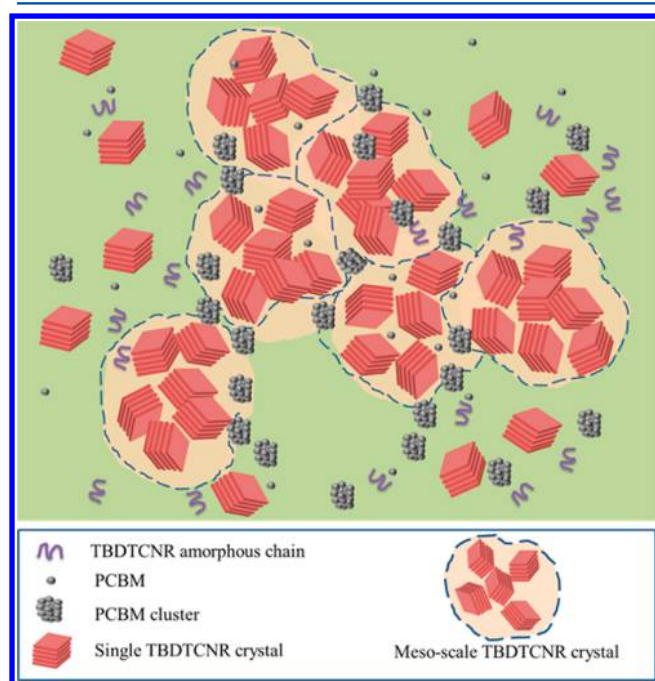
Figure 3. Schematic representations of multilength-scale BHJ structures in TBDTCNR:$PC_{61}BM$ blend films, including (1) nanoscale $PC_{61}BM$ clusters, (2) nanoscale single SM crystallites, (3) mesoscale primary SM crystallites (circled by blue dashed line), (4) a fractal-like network (circled by blue dashed line) formed by the aggregation of primary SM crystallites, and (5) an amorphously miscible matrix (green area).

The GISAXS intensity contributed by the morphology of the fractal network structure of the SM crystallites (at multiple length scales) can be expressed as

$$I_{SM}(Q) = P(Q) \times S(Q) \tag{2}$$

where $P(Q)$ is the form factor of the primary SM particles (approximated by a spherical shape having a mean radius R_{SM}) and $S(Q)$ is the fractal structure factor describing the interaction between the primary SM particles in this fractal-like aggregation system. $P(Q)$ includes a prefactor (proportional to the intensity scale) that is the product of the particle volume fraction φ and the square of the scattering length density contrast between SM crystallites. $S(Q)$ is given by[56,57]

$$S(Q) = 1 + \frac{\sin[(D-1)\tan^{-1}(Q\xi)]}{(QR_{SM})^D}$$
$$\times \frac{D\Gamma(D-1)}{[1 + 1/(Q\xi)^2]^{(D-1)/2}} \tag{3}$$

where ξ is the characteristic length of the fractal-like network (or domain) formed through aggregation of the primary particles and D is the fractal dimension. $\Gamma(x)$ is the gamma function of argument x. The least-squares fitting of eq 2 takes into account the polydispersity, p_{SM}, of the primary SM particles having a Schulz size distribution. Notably, the volume fractions φ determined herein are only for relative comparison; they are not absolute values because we could not measure the absolute values of the scattering contrast from the GISAXS experiments.

To simultaneously resolve the structures of the $PC_{61}BM$ clusters and the fractal network (fractal-like aggregation) of SM crystallites, we modeled the measured GISAXS profiles using the equation

$$I(Q) = I_{PCBM}(Q) + I_{SM}(Q) + b \tag{4}$$

The constant b represents the incoherent scattering background. Figure 1 reveals that the measured GISAXS profile of the TBDTCNR:$PC_{61}BM$ (1:0.4) blend film could be fitted[48] well using the model of eq 4. The $I_{PCBM}(Q)$ and $I_{SM}(Q)$ models dominated independently at different Q ranges. The former, for the PCBM clusters, dominated in the mid-Q region (0.008–0.03 Å^{-1}), as revealed by the characteristic broad peak of the measured GISAXS profile. The latter, for the aggregation of primary SM crystallites, dominated in the low-Q region (0.003–0.008 Å^{-1}), as revealed by the upturn intensity of the measured GISAXS profile. The contributions of both models are separable (major parts do not overlap). Therefore, the two groups of parameters in the respective models were not affected by each other during the nonlinear least-squares calculation (Supporting Information). Basically, these fitted parameters are reliable. Table 1 lists the structural parameters η, R, p, φ, R_{SM}, p_{SM}, D, and ξ, extracted by the model-fitting. Interestingly, the radius (10.4 nm) of the $PC_{61}BM$ clusters for the SM/$PC_{61}BM$ blend film prepared without thermal annealing was similar to those of $PC_{61}BM$ clusters in optimal thermally annealed P3HT/$PC_{61}BM$ blend films,[16,20,33] revealing quantitative information about the optimal $PC_{61}BM$ cluster structure. The mean radius of the primary SM crystallites formed through closely packed aggregation of single SM crystals having a size of 17 nm (from GIWAXS data) was 44.6 nm. The determined values of ξ (ca. 300 nm) are outside the range corresponding to the taken Q range (Q_{min} = 0.003 Å^{-1}). The determined values

Table 1. Structural Parameters Determined through SAXS Model Fitting for TBDTCNR:PC$_{61}$BM Films (Blend Ratio = 1:0.4) Annealed at Various Temperatures

anneal temp (°C)	η (%)	R (nm)	p	R_{SM} (nm)	p_{SM}	D	ξ (nm)
room temp	16.1	10.4	0.26	44.6	0.27	2.36	280
75	20.2	12.2	0.25	49.2	0.26	2.33	319
100	15.2	16.2	0.29	54.5	0.29	2.11	327
125	15.0	24.5	0.41	–	–	–	–

of ξ had large uncertainties, which are caused by the model fitting that uses an extrapolation. Roughly speaking, all the values of ξ should be corrected as ">300 nm." The domain size of a fractal-like network can be characterized approximately by the Guinier radius (i.e., the radius of gyration):[56]

$$R_g = [D(D + 1)/2]^{1/2}\xi \qquad (5)$$

The Guinier radius of the fractal-like network domain was > 560 nm. The SAXS technique is particularly applicable for characterizing fractal-like aggregation structures using the power-law scattering behavior.[52−56] GISAXS can provide information complementary to the data obtained from TEM and AFM local observations (Figure 4). In Figure 4b, the local
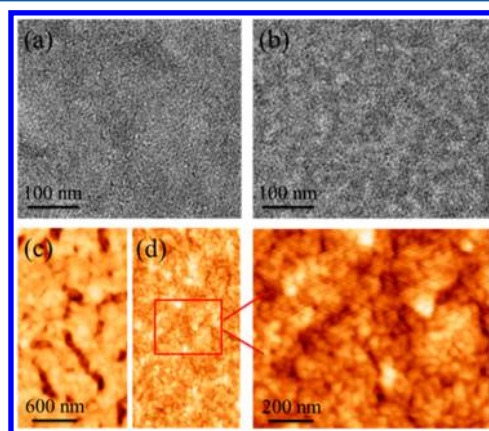
Figure 4. (a, b) TEM images of (a) the pristine SM film and (b) the SM/PC61BM blend film (blend ratio =1:0.4); light and dark colors represent the SM and PC61BM phases, respectively; the contrast between parts a and b reveals overlapping of nanoscale PC61BM clusters. (c, d) AFM topographic images of (c) the pristine SM film, revealing the fractal surface of the micrometer-scale SM particles, and (d) the SM/PC61BM blend film, revealing the close aggregation of nanoscale single SM crystallites into mesoscale primary particles and the further aggregation of the primary particles.

morphology observed through TEM is characteristic of a fractal-like object. In Figure 4, parts c and 4d, the AFM images of the surface morphology of the film also reveal the aggregation of primary SM crystallites from the mesoscale to macroscale. Each SM crystallite comprised nanoscale single SM crystals. These results also provides insight into the 3D frameworks of BHJ structures, interpenetration networks, and SM crystallites in general SMOSCs on the nano- and mesoscales observed through AFM and TEM.[6,29−32,58]

3.3. Mechanism of Structural Evolution Tuned by PC$_{61}$BM Content and Annealing Temperature. When the content of PC$_{61}$BM in the blend increased from 1:0.4 to 1:0.9, the structures of the PC$_{61}$BM clusters and fractal-like network (in the investigated scale range) of SM crystallites did not change appreciably, as evidenced by the GISAXS profiles in

Figure 1. These observations suggest that after the nanoscale PC$_{61}$BM cluster had formed, any additional PC$_{61}$BM molecules (in the cases where the blend ratio was greater than 1:0.4) would tend to be miscible with SMs in the amorphous matrix. In addition to the factor of PC$_{61}$BM solubility, this phenomenon can be explained as follows. The kinetics of formation of the SM crystallites in the blend solution was faster than that of the PC$_{61}$BM clusters. Thus, the spatial distribution of the formed SM crystallites limited or hindered any subsequent PC$_{61}$BM clustering. On the other hand, the increase in the content of PC$_{61}$BM molecules dispersed in the miscible matrix domain also affected or destroyed the nucleation sites of SM crystallization, decreasing the number of SM crystallites dispersed in the matrix (consistent with our observations in the previous section).

Figure 1b displays the in-plane GISAXS profiles of the TBDTCNR:PC$_{61}$BM (1:0.4) blend films after experiencing different annealing temperatures. The size of the PC$_{61}$BM clusters increased substantially upon increasing the annealing temperature, as evidenced by the shift of the medium-Q peak toward the high-Q region. Table 1 list the quantitative data obtained from analysis of the GISAXS model. The relative volume fraction of PC$_{61}$BM clusters remained unchanged upon increasing the temperature, but the radius of the PC$_{61}$BM clusters grew from 10.4 to 24.5 nm, suggesting the late stage of a typical growth step. The corresponding crystallinity (or number of single SM crystallites) increased significantly upon increasing the annealing temperature, as indicated by the relative peak intensities in Figure 5. According to Table 1, the radius of primary SM crystallites also increased from 44.6 nm at room temperature to 54.5 nm after annealing at 100 °C, consistent with the aggregation of more single crystallites into the primary particle. In addition, the fractal dimension decreased accordingly, from 2.36 to 2.1, suggesting dense, 2D-like structural packing of the primary SM particles. Because of the limit of the lowest value of Q (<0.001 Å^{-1}) in the intensity profile, uncertainties in determining the sizes of the large domains and the increases in the number of primary particles occurred with the loss of low-Q intensity upon shifting of this peak. For the film that had been annealed at 125 °C, the low-Q GISAXS intensity corresponding to the large fractal-like SM domain developed toward the lowest value of Q and was beyond our measurement capabilities; we could not obtain accurate information regarding the large SM domain and, therefore, we mainly fit the GISAXS peak corresponding to the PC$_{61}$BM clusters in this case.

We were interested in exploring the mutual interactions of or confinement between SM crystallization and PC$_{61}$BM clustering with respect to the annealing temperature of the blend film. Here, the maximum radius of the nanoscale PC$_{61}$BM clusters (ca. 24 nm) for the SMOSCs was much larger than that of well-known P3HT/PC$_{61}$BM PSCs (ca. 10 nm).[16,33,37] In addition, the upper limit of the growth of the PC$_{61}$BM clusters (ca. 10 nm) in the P3HT/PC$_{61}$BM PSC was not sensitive to the
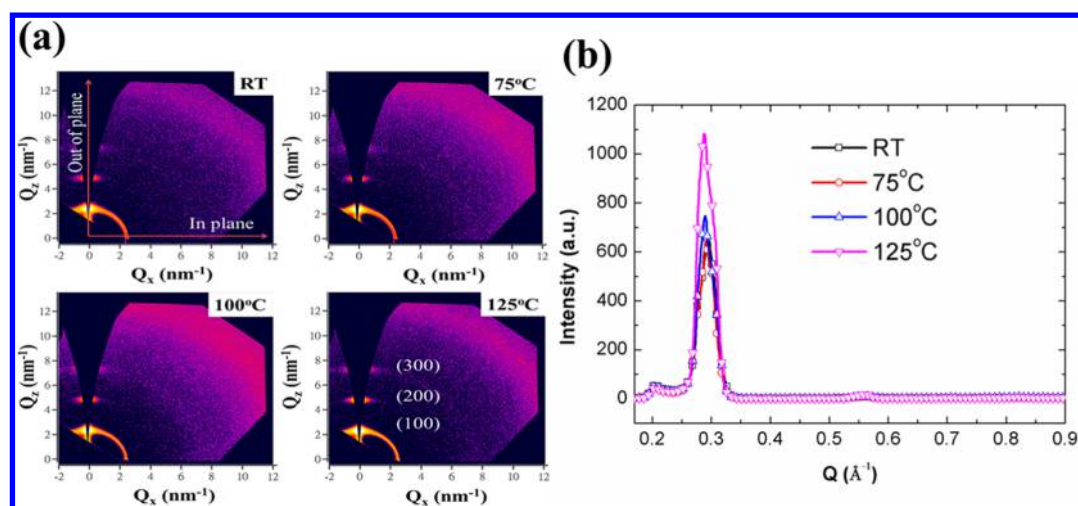
Figure 5. (a) 2D GIWAXS patterns and (b) ring-averaged GIWAXS profiles for TBDTCNR:PC$_{61}$BM blend films annealed at room temperature and 75, 100, and 125 °C.

commonly employed annealing temperature.[37] These two features reveal a discrepancy between the mechanisms of PC$_{61}$BM clustering in the PSCs and SMOSCs. It was clear that the thermal and spatial diffusions of PC$_{61}$BM molecules were not limited by the SM crystal network or single crystallites in the amorphous matrix upon elevating the annealing temperature. We deduce that, at higher temperatures, the rate of diffusion of PC$_{61}$BM molecules in the matrix into the clusters was higher than (i) the aggregation of mesoscale primary SM particles into large fractal-like crystals or (ii) aggregation of single SM crystals into primary particles. The growth of PC$_{61}$BM clusters or the depletion of individual PC$_{61}$BM molecules in the amorphous matrix resulted in spaces in the matrix available for nucleation of single SM crystals and for extension of the fractal-like network (as determined through GISAXS analysis), leading to subsequent enhancement in SM crystallization. These hypotheses are confirmed when considering the concurrent GIWAXS profiles in Figure 5(b), revealing that the intensity of the (100) diffraction peak of the single SM crystallites increased upon increasing the annealing temperature; if it did not, the mesoscale or large fractal-like SM crystallites formed earlier would have spatially confined the growth of PC$_{61}$BM clusters, much like the thermal behavior of PC$_{61}$BM clusters in P3HT/PC$_{61}$BM PSCs.[20,59] Thus, our present study suggests that fractal-like aggregation and the formation of SM primary particles play important roles in inducing the different phase-separation mechanisms of SMOSCs from that of PSCs. Accordingly, we conclude that nanoscale PC$_{61}$BM clustering in the SMOSC could be tuned by varying the annealing temperature, rather than by varying the amount of incorporated PC$_{61}$BM in the film.

3.4. Ordered Molecular Stacking and Angular Distribution of Nanoscale SM Crystallites in TBDTCNR/PC$_{61}$BM Blend Films.

The out-of-plane GIWAXS profiles for the blend and pristine films (Figure 2b) revealed high crystallinity with ordered molecular packing for TBDTCNR. On the basis of the theoretical molecular architecture (Figure 6), the [001], [010], and [100] stacking directions are defined as the orientations along the directions of the backbone, the π–π stacks, and the alkyl side chain.[30,59] Along the direction of the alkyl chain, there is apparently high ordering, as indicated by the (100) and (200) diffraction spots (marked in Figure 2a)
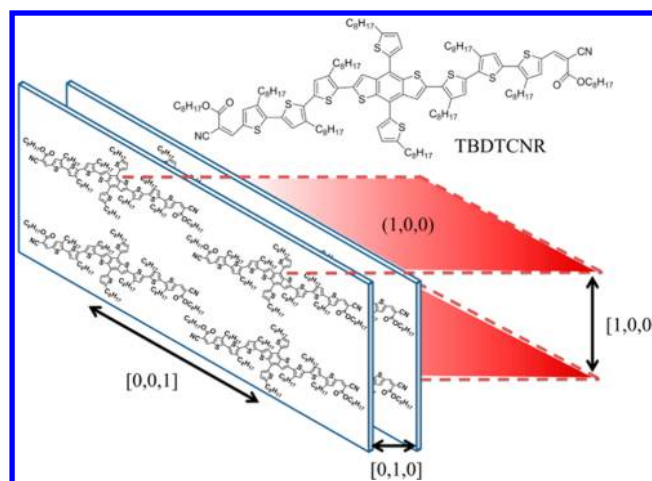
Figure 6. Molecular structure of TBDTCNR and the ordered molecular stacking of TBDTCNR in the crystal, revealing the three orthogonal directions with respect to the molecular architecture.

and peaks (Figure 2b). The single SM crystals possessed a lamellar structure with ordered (100) layers. We determined an interlayer spacing of 21.4 Å from the position of the (100) diffraction peak at a value of Q of 0.294 Å^{-1}, consistent with data reported previously.[32] We also found evidence for a (001) diffraction peak at a value of Q of 0.206 Å^{-1}, indicating ordering along the backbone direction; the interspacing between (001) planes (30.50 Å) was consistent with the length of the backbone of TBDTCNR. Figure 2b displays the ordered 2D stacking constructed along the [001] and [100] direction.

Crystallites in which the orientation of the (100) lamellar layer is parallel to a film surface are usually defined as "edge-on" (in this case, the edge of the thiophene ring in the backbone is "on"). Information about edge-on crystallites is mainly determined from out-of-plane GIWAXS profiles. Similarly, in-plane GIWAXS profiles (marked in Figure 2a) mainly reveal information about face-on crystallites with the (100) lamellar layer perpendicular to the film surface (in this case, the face of the thiophene ring is "on"). The orientation of edge-on SM crystallites has a certain angular distribution (see the bright arc-like spots in 2D GIWAXS pattern). In addition to edge- and

Table 2. Performance and Mobility of SMOSC Devices Incorporating the Investigated Films[a]

active layer	J_{sc} (mA cm^{-2})	V_{oc} (V)	FF	PCE (%)	μ_h (cm^2 V^{-1} s^{-1})	μ_e (cm^2 V^{-1} s^{-1})
1:0.4 @ room temp	8.89 ± 0.10 (9.06)	0.904 ± 0.005 (0.91)	0.656 ± 0.005 (0.65)	5.27 ± 0.07 (5.36)	1.31×10^{-4}	1.26×10^{-4}
1:0.75 @ room temp	5.77 ± 0.13 (6.01)	0.859 ± 0.006 (0.86)	0.521 ± 0.006 (0.52)	2.58 ± 0.07 (2.69)	9.45×10^{-5}	2.06×10^{-4}
1:0.9 @ room temp	3.52 ± 0.11 (3.63)	0.800 ± 0.008 (0.81)	0.473 ± 0.007 (0.48)	1.33 ± 0.04 (1.41)	6.82×10^{-5}	2.80×10^{-4}
1:0.4 @ 75 °C	6.37 ± 0.12 (6.41)	0.869 ± 0.012 (0.87)	0.637 ± 0.007 (0.65)	3.53 ± 0.05 (3.62)	1.20×10^{-4}	9.60×10^{-5}
1:0.4 @ 100 °C	3.99 ± 0.20 (4.24)	0.811 ± 0.011 (0.82)	0.469 ± 0.010 (0.47)	1.52 ± 0.06 (1.63)	7.04×10^{-5}	5.97×10^{-5}
1:0.4 @ 125 °C	0.89 ± 0.06 (0.91)	0.707 ± 0.013 (0.72)	0.313 ± 0.015 (0.33)	0.20 ± 0.01 (0.22)	5.10×10^{-5}	4.07×10^{-5}

[a]The data are averaged over 10 devices, and the highest performances are presented in parentheses.

face-on crystallites, some SM crystallites are isotropic, demonstrated by the white ring.

The area of the out-of-plane (100) diffraction peak was seven times greater than that of the in-plane (100) diffraction peak. Therefore, the edge-on crystallites dominated the structure, providing a pathway for hole transport along the [100] direction of the edge-on crystallites (i.e., perpendicular to the film surface); hole transport along the [010] (π–π stacking) direction of the edge-on crystallites (parallel to the film surface) would be relatively minor. The diffraction peak representing ordering along the π–π stacking direction of edge-on crystallites was too weak to be detected in our in-plane GIWAXS profiles. For the minor phase of face-on crystallites, the hole mobility could be enhanced due to the facilitated hole transport along the π–π stacking direction (perpendicular to the film surface) to the electrode. Improving the orientation of single SM crystals for hole transport perpendicular to the film surface may be an important issue in future studies. In essence, the out-of-plane GIWAXS profiles featured a similar evolution in response to the content of PC$_{61}$BM as did those of the ring-averaged GIWAXS profiles (Figure 2d).

Interestingly, upon increasing the content of PC$_{61}$BM, a fraction of the edge-on crystallites changed their orientation to the isotropic and face-on orientations. Figure 2a displays qualitatively the shrinkage of a spot of a (100) lamellar layer of edge-on crystallites (in the out-of-plane direction), accompanied by the formation and growth of isotropic and face-on crystallites (along the ring direction). Parts b and c of Figure 2 reveal that, upon the content of PC$_{61}$BM is increased, the decrease in the (100) peak intensity of edge-on crystallites corresponds quantitatively to the increase in the (100) peak intensity of face-on crystallites. We suspect that the partial transformation in orientation from edge-on to face-on and isotropic SM crystallites was caused by (i) the increase in the number of PC$_{61}$BM molecules dispersed in the amorphous matrix and (ii) the independent formation of face- and edge-on SM crystallites (as discussed in section 3.4). In addition to decreasing the relative crystallinity, the transformation in orientation might have had some effects on the hole mobility. The intensity of the (100) peak at a blend ratio of 1:0.75 was slightly higher than that at 1:0.9, possibly because of a variance in local thickness.

The 2D GIWAXS patterns in Figure 5a of the TBDTCNR/PC$_{61}$BM (1:0.4) blend films that had been annealed at room temperature and 75, 100, and 125 °C indicate that the transformation of the orientation of the crystallites from the edge-on to the face-on or isotropic state was independent of the annealing temperatures. As revealed in Figure 5b, the azimuthally integrated intensity of the (100) peak increased upon increasing the annealing temperature, suggesting that SM crystallization was enhanced significantly at elevated temperature. In contrast, the orientation of the nanoscale SM

crystallites was dependent on the content of PC$_{61}$BM dispersed in the matrix.

3.5. Relationships among Structure, Photovoltaic Properties, and Performance for TBDTCNR/PC$_{61}$BM OSCs. A BHJ structure providing optimal photovoltaic performance should exhibit two main features: (i) nanoscale miscibility that provides efficient exciton dissociation at the well-intermixed interfaces between SM crystals and PC$_{61}$BM and (ii) phase-separated SM crystals and PC$_{61}$BM domains that form an interpenetrating network (effective transport of electrons and holes along respective paths to their electrodes). Usually, a compromise must be reached between these two factors governing the photovoltaic properties of the active layer, leading to the development of several strategies for improving PCEs. Although a previous study revealed[32] that the optimal blend ratio of 1:0.4 provided a miscible structure and charge transport paths displaying the most balanced ratio of electron and hole mobilities (μ_e/μ_h), it did not provide any quantitative structural characterization at multiple length scales nor any correlation to performance or properties. In this present study, we examined the relationships among the structure, the photovoltaic properties, and performance. Table 2 lists the photovoltaic performance and electron and hole mobilities of the corresponding SMOSC-based devices incorporating all of the films investigated herein.

The incorporation of PC$_{61}$BM into the blend film dispersed the large micrometer-scale SM crystallites originally in the pristine SM film into a fractal-like network having dimension of approximately 2.3 (in the investigated scale range), due to the partial miscibility of the fullerene and the SM. The PC$_{61}$BM clusters formed with a size similar to that of optimally performing PSCs. The fractal-like SM crystal aggregation and PC$_{61}$BM clusters actually constituted the main interpenetrating network for charge transport. Notably, this structure does not depend on the blend ratio (≥0.4), as discussed in our analysis of the GISAXS data. According to Table 2, the PCE degraded upon increasing the blend ratio, mainly due to decreases in both the short-circuit current (J_{sc}) and fill factor (FF). Thus, increasing the number of nanoscale SM crystallites in the amorphous matrix was a critical factor, increasing the interfacial area between the acceptor and donor phases and optimizing the path of charge transport, consequently, enhancing the short-circuit current and the hole mobility in the device incorporating the optimal structure. The change in the orientation of the SM crystallites upon increasing the blend ratio may have contributed to the decrease in hole mobility. On the other hand, the number of PC$_{61}$BM molecules dispersed in the matrix (increasing upon increasing the blend ratio) was responsible for the increase in electron mobility. An imbalance in charge mobility (μ_e/μ_h) upon increasing the blend ratio would lead to greater recombination of charge carriers, thereby decreasing the FF. Notably, hole hopping between nanoscale SM crystallites

and electron hopping between $PC_{61}BM$ molecules in the matrix would also contribute to the mechanism of charge transport.[19,60−64] In future studies, in addition to a stable, optimal interpenetrating network (starting at a blend ratio of 1:0.4), we could adopt a strategy of increasing the number of nanoscale SM crystallites and decreasing the content of $PC_{61}BM$ in the matrix to improve the PCE.

When we annealed the film prepared at a blend ratio of 1:0.4, the sizes of the $PC_{61}BM$ clusters and primary SM particles grew upon increasing the annealing temperature. The interpenetrating phase-separated network that formed did not, however, facilitate the transport of the charge carriers, leading to decays in the values of μ_e and μ_h. Thus, the meso- or micrometer-scale SM crystallites and large $PC_{61}BM$ clusters could not form effective interpenetrated or interconnected networks, due to the growth of these species—albeit difficult to observe using microscopic tools. On the other hand, we deduced that electron hopping between $PC_{61}BM$ molecules and hole hopping between nanoscale SM crystallites in the amorphous matrix may have contributed to the mobility to a certain degree. We attribute the large decrease in FF to (i) the lower values of μ_e and μ_h and (ii) the increase in the probability of recombination caused by the presence of defect traps, due to the contribution of carrier hopping in the matrix. The large decrease in the value of J_{sc} was presumably due mainly to the decrease in the interfacial surfaces. Overall, the PCE decayed dramatically after structural evolution induced by the elevated temperature.

4. CONCLUSION

We have used simultaneous GISAXS/GIWAXS measurements to quantitatively elucidate the multilength-scale BHJ structures of SMOSCs comprising 2D- and fractal-like networks of SM crystallites and nanoscale $PC_{61}BM$ clusters at multiple length scales. We found that the BHJ structure of an SMOSC is different from that of a PSC because of relatively rapid SM crystallization, distinctive SM crystallization behavior, and mutual interactions between the SM and $PC_{61}BM$. For instance, the distinctive phase-separation behavior in an SM structure can be tuned by varying the content of incorporated $PC_{61}BM$ and the annealing temperature; we have performed a fundamental investigation of the mechanism behind the mutual interactions of $PC_{61}BM$ aggregation and SM crystallization that constitute different interpenetrating networks, which form the pathways for charge transport. Moreover, in addition to the formation of meso- and macroscale interpenetrated and phase-separated networks, we found that electron hopping between $PC_{61}BM$ molecules and hole hopping between nanoscale SM crystallites in the amorphous matrix could also contribute to the photovoltaic properties and performance. We also probed the additive effect on the morphology and device performance of $SM/PC_{71}BM$ OSCs with GIWAXS and elucidated a different mechanism for the $PC_{71}BM$ case from the $PC_{61}BM$ case, thus providing a comprehensive comparison of SMOSCs based on $PC_{61}BM$ and $PC_{71}BM$, respectively, as acceptors. This study provides a fundamental understanding of the factors influencing the synthesis, design, and performance of SMOSCs.

ASSOCIATED CONTENT

ⓈSupporting Information
Performance of devices based on TBDTCNR and $PC_{71}BM$ blend films processed with additive, GIWAXS profiles of TBDTCNR/$PC_{61}BM$ active layer on the Si/PEDOT:PSS and Si substrate, respectively, the GISAXS intensities calculated

from two submodels in comparison to the fitted intensity, and pole figure of GIWAXS. The Supporting Information is available free of charge on the ACS Publications website at DOI: 10.1021/acs.jpcc.5b05239.

AUTHOR INFORMATION

Corresponding Authors
*(C.-S.T.) E-mail: cstsao@iner.gov.tw;.
*(C.-W.C.) E-mail: gchu@gate.sinica.edu.tw.

Notes
The authors declare no competing financial interest.

REFERENCES

(1) Darling, S. B.; You, F. The Case for Organic Photovoltaics. *RSC Adv.* **2013**, *3*, 17633−17648.

(2) Li, G.; Zhu, R.; Yang, Y. Polymer Solar Cells. *Nat. Photonics* **2012**, *6*, 153−161.

(3) Gendron, D.; Leclerc, M. New Conjugated Polymers for Plastic Solar Cells. *Energy Environ. Sci.* **2011**, *4*, 1225−1237.

(4) Facchetti, A. π-Conjugated Polymers for Organic Electronics and Photovoltaic Cell Applications. *Chem. Mater.* **2011**, *23*, 733−758.

(5) Kyaw, A. K. K.; Wang, D. H.; Gupta, V.; Zhang, J.; Chand, S.; Bazan, G. C.; Heeger, A. J. Efficient Solution-Processed Small-Molecule Solar Cells with Inverted Structure. *Adv. Mater.* **2013**, *25*, 2397−2402.

(6) Zhou, J.; Zuo, Y.; Wan, X.; Long, G.; Zhang, Q.; Ni, W.; Liu, Y.; Li, Z.; He, G.; Li, C.; Kan, B.; Li, M.; Chen, Y. Solution-Processed and High-Performance Organic Solar Cells Using Small Molecules with a Benzodithiophene Unit. *J. Am. Chem. Soc.* **2013**, *135*, 8484−8487.

(7) Wang, D. H.; Kyaw, A. K. K.; Gupta, V.; Bazan, G. C.; Heeger, A. J. Enhanced Efficiency Parameters of Solution-Processable Small-Molecule Solar Cells Depending on ITO Sheet Resistance. *Adv. Energy Mater.* **2013**, *3*, 1161−1165.

(8) He, Z.; Zhong, C.; Su, S.; Xu, M.; Wu, H.; Cao, Y. Enhanced Power-Conversion Efficiency in Polymer Solar Cells Using an Inverted Device Structure. *Nat. Photonics* **2012**, *6*, 591−595.

(9) Nikiforov, M. P.; Lai, B.; Chen, W.; Chen, S.; Schaller, R. D.; Strzalka, J.; Maser, J.; Darling, S. B. Detection and Role of Trace Impurities in High-Performance Organic Solar Cells. *Energy Environ. Sci.* **2013**, *6*, 1513−1520.

(10) Mishra, A.; Bäuerle, P. Small Molecule Organic Semiconductors on the Move: Promises for Future Solar Energy Technology. *Angew. Chem., Int. Ed.* **2012**, *51*, 2020−2067.

(11) Sun, Y.; Welch, G. C.; Leong, W. L.; Takacs, C. J.; Bazan, G. C.; Heeger, A. J. Solution-Processed Small-Molecule Solar Cells with 6.7% Efficiency. *Nat. Mater.* **2012**, *11*, 44−48.

(12) Ma, W.; Yang, C.; Gong, X.; Lee, K.; Heeger, A. J. Thermally Stable, Efficient Polymer Solar Cells with Nanoscale Control of the Interpenetrating Network Morphology. *Adv. Funct. Mater.* **2005**, *15*, 1617−1622.

(13) Andersson, B. V.; Herland, A.; Masich, S.; Inganäs, O. Imaging of the 3D Nanostructure of a Polymer Solar Cell by Electron Tomography. *Nano Lett.* **2009**, *9*, 853−855.

(14) van Bavel, S. S.; Sourty, E.; de With, G.; Loos, J. Three-Dimensional Nanoscale Organization of Bulk Heterojunction Polymer Solar Cells. *Nano Lett.* **2009**, *9*, 507−513.

(15) Chen, W.; Xu, T.; He, F.; Wang, W.; Wang, C.; Strzalka, J.; Liu, Y.; Wen, J.; Miller, D. J.; Chen, J.; Hong, K.; Yu, L.; Darling, S. B. Hierarchical Nanomorphologies Promote Exciton Dissociation in Polymer/Fullerene Bulk Heterojunction Solar Cells. *Nano Lett.* **2011**, *11*, 3707−3713.

(16) Liao, H.-C.; Tsao, C.-S.; Lin, T.-H.; Chuang, C.-M.; Chen, C.-Y.; Jeng, U. S.; Su, C.-H.; Chen, Y.-F.; Su, W.-F. Quantitative Nanoorganized Structural Evolution for a High Efficiency Bulk Heterojunction Polymer Solar Cell. *J. Am. Chem. Soc.* **2011**, *133*, 13064−13073.

(17) Liao, H.-C.; Tsao, C.-S.; Shao, Y.-T.; Chang, S.-Y.; Huang, Y.-C.; Chuang, C.-M.; Lin, T.-H.; Chen, C.-Y.; Su, C.-J.; Jeng, U. S.; Chen, Y.-F.; Su, W.-F. Bi-hierarchical Nanostructures of Donor-acceptor Copolymer and Fullerene for High Efficient Bulk Heterojunction Solar Cells. *Energy Environ. Sci.* **2013**, *6*, 1938−1948.

(18) Liao, H. C.; Tsao, C. S.; Huang, Y. C.; Jao, M. H.; Tien, K. Y.; Chuang, C. M.; Chen, C. Y.; Su, C. J.; Jeng, U.-S.; Chen, Y. F.; Su, W. F. Insight of Solvent Vapor Annealing on the Performance of Bulk Heterojunction Solar Cell by Quantitative Nanomorphology Study. *RSC Adv.* **2014**, *4*, 6246−6253.

(19) Kiel, J. W.; Eberle, A. P. R.; Mackay, M. E. Nanoparticle Agglomeration in Polymer-based Solar Cells. *Phys. Rev. Lett.* **2010**, *105*, 168701.

(20) Wu, W.-R.; Jeng, U.-S.; Su, C.-J.; Wei, K.-H.; Su, M.-S.; Chiu, M.-Y.; Chen, C.-Y.; Su, W.-B.; Su, C.-H.; Su, A.-C. Competition between Fullerene Aggregation and Poly(3-hexylthiophene) Crystallization upon Annealing of Bulk Heterojunction Solar Cells. *ACS Nano* **2011**, *5*, 6233−6243.

(21) He, F.; Wang, W.; Chen, W.; Xu, T.; Darling, S. B.; Strzalka, J.; Liu, Y.; Yu, L. Tetrathienoanthracene-based Copolymers for Efficient Solar Cells. *J. Am. Chem. Soc.* **2011**, *133*, 3284−3287.

(22) Lou, S. J.; Szarko, J. M.; Xu, T.; Yu, L.; Marks, T. J.; Chen, L. X. Effects of Additives on the Morphology of Solution Phase Aggregates Formed by Active Layer Components of High-Efficiency Organic Solar Cells. *J. Am. Chem. Soc.* **2011**, *133*, 20661−20663.

(23) Farahat, M. E.; Wei, H.-Y.; Ibrahem, M. A.; Boopathi, K. M.; Wei, K.-H.; Chu, C.-W. A Dual-functional Additive Improves the Performance of Molecular Bulk Heterojunction Photovoltaic Cells. *RSC Adv.* **2014**, *4*, 9401−9411.

(24) Liu, C.-M.; Su, Y.-W.; Jiang, J.-M.; Chen, H.-C.; Lin, S.-W.; Su, C.-J.; Jeng, U. S.; Wei, K.-H. Complementary Solvent Additives Tune the Orientation of Polymer Lamellae, Reduce the Sizes of Aggregated Fullerene Domains, and Enhance the Performance of Bulk Heterojunction Solar Cells. *J. Mater. Chem. A* **2014**, *2*, 20760−20769.

(25) Su, M.-S.; Kuo, C.-Y.; Yuan, M.-C.; Jeng, U.-S.; Su, C.-J.; Wei, K.-H. Improving Device Efficiency of Polymer/Fullerene Bulk Heterojunction Solar Cells Through Enhanced Crystallinity and Reduced Grain Boundaries Induced by Solvent Additives. *Adv. Mater.* **2011**, *23*, 3315−3319.

(26) Lan, S.-C.; Raghunath, P.; Lu, Y.-H.; Wang, Y.-C.; Lin, S.-W.; Liu, C.-M.; Jiang, J.-M.; Lin, M.-C.; Wei, K.-H. Symmetry and Coplanarity of Organic Molecules Affect their Packing and Photovoltaic Properties in Solution-Processed Solar Cells. *ACS Appl. Mater. Interfaces* **2014**, *6*, 9298−9306.

(27) Zhou, H.; Zhang, Y.; Mai, C.-K.; Seifter, J.; Nguyen, T.-Q.; Bazan, G. C.; Heeger, A. J. Solution-Processed pH-Neutral Conjugated Polyelectrolyte Improves Interfacial Contact in Organic Solar Cells. *ACS Nano* **2015**, *9*, 371−377.

(28) Takacs, C. J.; Collins, S. D.; Love, J. A.; Mikhailovsky, A. A.; Wynands, D.; Bazan, G. C.; Nguyen, T.-Q.; Heeger, A. J. Mapping Orientational Order in a Bulk Heterojunction Solar Cell with Polarization-Dependent Photoconductive Atomic Force Microscopy. *ACS Nano* **2014**, *8*, 8141−8151.

(29) Shen, S.; Jiang, P.; He, C.; Zhang, J.; Shen, P.; Zhang, Y.; Yi, Y.; Zhang, Z.; Li, Z.; Li, Y. Solution-Processable Organic Molecule Photovoltaic Materials with Bithienyl-benzodithiophene Central Unit and Indenedione End Groups. *Chem. Mater.* **2013**, *25*, 2274−2281.

(30) Huang, J.; Zhan, C.; Zhang, X.; Zhao, Y.; Lu, Z.; Jia, H.; Jiang, B.; Ye, J.; Zhang, S.; Tang, A.; Liu, Y.; Pei, Q.; Yao, J. Solution-Processed DPP-Based Small Molecule that Gives High Photovoltaic Efficiency with Judicious Device Optimization. *ACS Appl. Mater. Interfaces* **2013**, *5*, 2033−2039.

(31) Liu, Y.; Wan, X.; Wang, F.; Zhou, J.; Long, G.; Tian, J.; Chen, Y. High-Performance Solar Cells using a Solution-Processed Small Molecule Containing Benzodithiophene Unit. *Adv. Mater.* **2011**, *23*, 5387−5391.

(32) Patra, D.; Huang, T.-Y.; Chiang, C.-C.; Maturana, R. O. V.; Pao, C.-W.; Ho, K.-C.; Wei, K.-H.; Chu, C.-W. 2-Alkyl-5-thienyl-Substituted Benzo[1,2-b:4,5-b′]dithiophene-Based Donor Molecules for Solution-Processed Organic Solar Cells. *ACS Appl. Mater. Interfaces* **2013**, *5*, 9494−9500.

(33) Huang, Y.-C.; Tsao, C.-S.; Chuang, C.-M.; Lee, C.-H.; Hsu, F.-H.; Cha, H.-C.; Chen, C.-Y.; Lin, T.-H.; Su, C.-J.; Jeng, U. S.; Su, W.-F. Small- and Wide-Angle X-ray Scattering Characterization of Bulk Heterojunction Polymer Solar Cells with Different Fullerene Derivatives. *J. Phys. Chem. C* **2012**, *116*, 10238−10244.

(34) Collins, B. A.; Tumbleston, J. R.; Ade, H. Miscibility, Crystallinity, and Phase Development in P3HT/PCBM Solar Cells: Toward an Enlightened Understanding of Device Morphology and Stability. *J. Phys. Chem. Lett.* **2011**, *2*, 3135−3145.

(35) Chen, W.; Nikiforov, M. P.; Darling, S. B. Morphology Characterization in Organic and Hybrid Solar Cells. *Energy Environ. Sci.* **2012**, *5*, 8045−8074.

(36) Rivnay, J.; Mannsfeld, S. C. B.; Miller, C. E.; Salleo, A.; Toney, M. F. Quantitative Determination of Organic Semiconductor Microstructure from the Molecular to Device Scale. *Chem. Rev.* **2012**, *112*, 5488−5519.

(37) Chen, C.-Y.; Tsao, C.-S.; Huang, Y.-C.; Liu, H.-W.; Chiu, W.-Y.; Chuang, C.-M.; Jeng, U. S.; Su, C.-J.; Wu, W.-R.; Su, W.-F.; Wang, L. Mechanism and Control of Structural Evolution of Polymer Solar Cell from Bulk Heterojunction to Thermally Unstable Hierarchical Structure. *Nanoscale* **2013**, *5*, 7629−7638.

(38) Perez, L. A.; Chou, K. W.; Love, J. A.; van der Poll, T. S.; Smilgies, D.-M.; Nguyen, T.-Q.; Kramer, E. J.; Amassian, A.; Bazan, G. C. Solvent Additive Effects on Small Molecule Crystallization in Bulk Heterojunction Solar Cells Probed During Spin Casting. *Adv. Mater.* **2013**, *25*, 6380−6384.

(39) Sharenko, A.; Kuik, M.; Toney, M. F.; Nguyen, T.-Q. Crystallization-Induced Phase Separation in Solution-Processed Small Molecule Bulk Heterojunction Organic Solar Cells. *Adv. Funct. Mater.* **2014**, *24*, 3543−3550.

(40) Shen, X. X.; Han, G. C.; Fan, D.; Xie, Y. J.; Yi, Y. P. Hot Charge-Transfer States Determine Exciton Dissociation in the DTDCTB/C-60 Complex for Organic Solar Cells: A Theoretical Insight. *J. Phys. Chem. C* **2015**, *119*, 11320−11326.

(41) Lee, C. K.; Pao, C. W. Nanomorphology Evolution of P3HT/PCBM Blends during Solution-Processing from Coarse-Grained Molecular Simulations. *J. Phys. Chem. C* **2014**, *118*, 11224−11233.

(42) Paek, S.; Choi, H.; Sim, J.; Song, K.; Lee, J. K.; Ko, J. Efficient Organic Solar Cells with Star-Shaped Small Molecules Comprising of Planar Donating Core and Accepting Edges. *J. Phys. Chem. C* **2014**, *118*, 27193−27200.

(43) Jageler-Hoheisel, T.; Selzer, F.; Riede, M.; Leo, K. Direct Electrical Evidence of Plasmonic Near-Field Enhancement in Small Molecule Organic Solar Cells. *J. Phys. Chem. C* **2014**, *118*, 15128−15135.

(44) Sharma, G. D.; Zervaki, G. E.; Angaridis, P. A.; Kitsopoulos, T. N.; Coutsolelos, A. G. Triazine-Bridged Porphyrin Triad as Electron Donor for Solution-Processed Bulk Hetero-Junction Organic Solar Cells. *J. Phys. Chem. C* **2014**, *118*, 5968−5977.

(45) Tan, Q.; Yang, X. C.; Cheng, M.; Wang, H. X.; Wang, X. N.; Sun, L. C. Application of Small Molecule Donor Materials Based on Phenothiazine Core Unit in Bulk Heterojunction Solar Cells. *J. Phys. Chem. C* **2014**, *118*, 16851−16855.

(46) Spencer, S.; Cody, J.; Misture, S.; Cona, B.; Heaphy, P.; Rumbles, G.; Andersen, J.; Collison, C. Critical Electron Transfer Rates for Exciton Dissociation Governed by Extent of Crystallinity in Small Molecule Organic Photovoltaics. *J. Phys. Chem. C* **2014**, *118*, 14840−16847.

(47) Liao, H.-C.; Ho, C.-C.; Chang, C.-Y.; Jao, M.-H.; Darling, S. B.; Su, W.-F. Additives for Morphology Control in High-efficiency Organic Solar Cells. *Mater. Today* **2013**, *16*, 326−336.

(48) Huo, L.; Zhang, S.; Guo, X.; Xu, F.; Li, Y.; Hou, J. Replacing Alkoxy Groups with Alkylthienyl Groups: A Feasible Approach To Improve the Properties of Photovoltaic Polymers. *Angew. Chem., Int. Ed.* **2011**, *50*, 9697−9702.

(49) Zhang, Q.; Kan, B.; Liu, F.; Long, G.; Wan, X.; Chen, X.; Zuo, Y.; Ni, W.; Zhang, H.; Li, M.; Hu, Z.; Huang, F.; Cao, Y.; Liang, Z.; Zhang, M.; Russell, T. P.; Chen, Y. Small-molecule Solar Cells with Efficiency Over 9%. *Nat. Photonics* **2015**, *9*, 35−41.

(50) Andersen, T. R.; Larsen-Olsen, T. T.; Andreasen, B.; Böttiger, A. P. L.; Carlé, J. E.; Helgesen, M.; Bundaard, E.; Norrman, K.; Andreasen, J. W.; Jørgensen, M.; Krebs, F. C. Aqueous Processing of Low-Band-Gap Polymer Solar Cells Using Roll-to-Roll Methods. *ACS Nano* **2011**, *5*, 4188−4196.

(51) Su, G. M.; Pho, T. V.; Eisenmenger, N. D.; Wang, C.; Wudl, F.; Kramer, E. J.; Chabinyc, M. L. Linking Morphology and Performance of Organic Solar Cells Based on Decacyclene Triimide Acceptors. *J. Mater. Chem. A* **2014**, *2*, 1781−1789.

(52) Schaefer, D. W. Polymers, Fractals, and Ceramic Materials. *Science* **1989**, *243*, 1023−1027.

(53) Schaefer, D.; Martin, J.; Wiltzius, P.; Cannell, D. Fractal Geometry of Colloidal Aggregates. *Phys. Rev. Lett.* **1984**, *52*, 2371−2374.

(54) Roe, R. J. *Methods of X-ray and Neutron Scattering in Polymer Science*; Oxford University Press: New York, 2000.

(55) Tsao, C. S.; Chuang, C. M.; Chen, C. Y.; Huang, Y. C.; Cha, H. C.; Hsu, F. H.; Chen, C. Y.; Tu, Y. C.; Su, W. F. Reaction Kinetics and Formation Mechanism of TiO2Nanorods in Solution: An Insight into Oriented Attachment. *J. Phys. Chem. C* **2014**, *118*, 26332−26340.

(56) Teixeira, J. Small-Angle Scattering by Fractal Systems. *J. Appl. Crystallogr.* **1988**, *21*, 781−785.

(57) Kline, S. R. Reduction and analysis of SANS and USANS data using IGOR Pro. *J. Appl. Crystallogr.* **2006**, *39*, 895−900.

(58) Wen, J.; Miller, D. J.; Chen, W.; Xu, T.; Yu, L.; Darling, S. B.; Zaluzec, N. J. Visualization of Hierarchical Nanodomains in Polymer/Fullerene Bulk Heterojunction Solar Cells. *Microsc. Microanal.* **2014**, *20*, 1507−1513.

(59) Verploegen, E.; Mondal, R.; Bettinger, C. J.; Sok, S.; Toney, M. F.; Bao, Z. Effects of Thermal Annealing Upon the Morphology of Polymer−Fullerene Blends. *Adv. Funct. Mater.* **2010**, *20*, 3519−3529.

(60) Lan, Y.-K.; Huang, C.-I. Charge Mobility and Transport Behavior in the Ordered and Disordered States of the Regioregular Poly(3-hexylthiophene). *J. Phys. Chem. B* **2009**, *113*, 14555−14564.

(61) Deibel, C.; Dyakonov, V. Polymer−Fullerene Bulk Heterojunction Solar Cells. *Rep. Prog. Phys.* **2010**, *73*, 096401.

(62) Campos, L. M.; Tontcheva, A.; Gunes, S.; Sonmez, G.; Neugebauer, H.; Sariciftci, N. S.; Wudl, F. Extended Photocurrent Spectrum of a Low Band Gap Polymer in a Bulk Heterojunction Solar Cell. *Chem. Mater.* **2005**, *17*, 4031−4033.

(63) Yu, D.; Park, K.; Durstock, M.; Dai, L. Fullerene-Grafted Graphene for Efficient Bulk Heterojunction Polymer Photovoltaic Devices. *J. Phys. Chem. Lett.* **2011**, *2*, 1113−1118.

(64) Maturová, K.; van Bavel, S. S.; Wienk, M. M.; Janssen, R. A. J.; Kemerink, M. Morphological Device Model for Organic Bulk Heterojunction Solar Cells. *Nano Lett.* **2009**, *9*, 3032−3037.